

$^{12}\text{C}(\gamma, p)^{11}\text{B}$ cross section from 80 to 157 MeV

P. D. Harty, J. C. McGeorge, I. J. D. MacGregor, R. O. Owens,
 J. R. M. Annand, I. Anthony, G. I. Crawford, S. N. Dancer,* S. J. Hall, J. D. Kellie, and G. J. Miller
Department of Physics and Astronomy, University of Glasgow, Glasgow G12 8QQ, Scotland

B. Schoch,[†] R. Beck, H. Schmieden, and J.M. Vogt[‡]
Institut für Kernphysik, Johannes-Gutenberg Universität, D-55099 Mainz, Germany

J. Ryckebusch

Laboratory for Nuclear Physics and Institute for Theoretical Physics, Proeftuinstraat 86, B-9000 Gent, Belgium

(Received 8 September 1994)

The $^{12}\text{C}(\gamma, p)^{11}\text{B}$ differential cross section has been measured over proton angles ranging from 58° to 128° , using tagged photons of energy 80–157 MeV, for low-lying regions of residual excitation energy in ^{11}B . The data have been compared with four different types of calculation. It is shown that scaling of the cross section with momentum mismatch occurs for both the ground-state and excited-state data.

PACS number(s): 25.20.-x, 27.20.+n

I. INTRODUCTION

In recent years there have been a number of tagged-photon measurements of the $^{12}\text{C}(\gamma, p)^{11}\text{B}$ differential cross section [1–6], in which the residual ^{11}B nucleus is left in a well-defined state or group of states. Combining these measurements with the early bremsstrahlung data of Matthews *et al.* [7] and proton-capture data on ^{11}B [8–10], there should now be an extensive data set with which to confront nuclear theories. However, the quoted systematic errors on these experiments range from 8–22%, and some discrepancies between the data sets are much larger, so that further data with a small systematic error can provide significant improvement to the knowledge of the cross section.

The theoretical situation for the $^{12}\text{C}(\gamma, N)$ reaction is also still rather unsatisfactory. It has been demonstrated [11–13] that calculations based on direct knockout (DKO) models do not adequately predict the cross section, both for (γ, p) and (γ, n) channels. A much better description of the data can be achieved [11–14] by incorporating the effects of meson-exchange currents (MEC) and the coupling of the initial and final states to the giant resonances. Despite the improved agreement between theories incorporating MEC and experiment, the calculations still do not give an adequate description of the measured differential cross section.

In this paper a measurement of the $^{12}\text{C}(\gamma, p)^{11}\text{B}$ differential cross section is reported, for which the resolution

was 3.5 MeV FWHM. This was sufficiently small to allow the cross section to small groups of states in the residual ^{11}B nucleus to be measured. For comparison with these cross sections, theoretical calculations have been performed for the photon energies of the present data.

II. EXPERIMENT

The experiment was performed using the Glasgow-Edinburgh-Mainz photon-tagging spectrometer [15] and the 183 MeV electron microtron at Mainz University (MAMI-A). An extensive description of the experimental arrangement has been given previously [16], and only a brief summary is given here.

The system was set up to tag photons with energies from 80 to 131 MeV in a first measurement, and energies from 131 to 157 MeV in a second. The tagging efficiency was measured with a large scintillating-glass detector placed directly in the photon beam, using a low beam intensity. The measured efficiency was stable and found to be ~ 0.65 at the higher range of photon energies, and ~ 0.58 for the lower range. The photon beam was collimated to a diameter of 33 mm at the target position. Timing coincidences between the proton detectors and residual electron detectors on the focal plane of the tagged photon spectrometer were recorded by six TDC's, each combining the signals from between 12 and 16 focal-plane detector channels.

The proton detection system consisted of a ΔE - E charged particle hodoscope [17] with a further 1 mm ΔE scintillator positioned 80 mm from the target, to provide particle identification information and a timing signal as part of the electronic trigger. The proton detector covered polar angles from 51° to 131° , with 3° resolution FWHM, and azimuthal angles from 70° to 110° with 5° resolution. The energy resolution was $\sim 5\%$ FWHM at

*Present address: Rolls Royce, Derby, United Kingdom.

[†]Present address: Physikalisches Institut, Universität Bonn, Bonn, Germany.

[‡]Present address: Saskatchewan Accelerator Laboratory, University of Saskatchewan, Saskatoon, Canada SN7 OWO.

70 MeV. The detector was positioned 0.45 m from the target, and covered 0.9 sr. The proton energy threshold of the E blocks in the detector was 8 MeV, corresponding to an effective threshold in the target of 28 MeV at 90° , increasing to 32 MeV at the extreme angles. The experimental trigger required a coincidence between all three ΔE - ΔE - E layers of the proton detector and the focal-plane detectors.

A natural graphite target, $152.5 \pm 0.8 \text{ mg cm}^{-2}$ thick, was positioned at 30° to the beam direction. Background data were taken with the target removed, and a perdeuterated polythene target (CD_2) of thickness $214.4 \pm 0.7 \text{ mg cm}^{-2}$ was used to obtain detector calibration data.

III. ANALYSIS AND RESULTS

The basic analysis procedure has been previously described [16], so that the main emphasis here will be on features particular to this experiment.

Protons were separated cleanly from other particles by selecting the appropriate regions in plots of ΔE versus E and E versus time of flight. Events near the ends of the scintillator blocks and at the extreme azimuthal angles of the detector were rejected, as these have poorer resolution. Events were discarded when there were multiple hits amongst the tagging electron detectors feeding the same TDC. A calculated correction factor [18] of ~ 1.2 was applied. Subtraction of random coincidences between the tagging electron detectors and proton detector was achieved in the manner described in Ref. [16].

In the present analysis, it is useful to display the data as a function of residual excitation energy in ^{11}B , defined as

$$E_x = E_\gamma - E_p - E_r + Q, \quad (1)$$

where E_γ is the photon energy, E_p is the proton kinetic energy, E_r is the kinetic energy of the recoiling system calculated from the photon and proton momenta, and Q is the Q value of the $^{12}\text{C}(\gamma, p)^{11}\text{B}$ reaction. The E_x spectra have been obtained from the data in five separate photon energy bins, $E_\gamma = 88 \pm 8, 106 \pm 9, 123 \pm 8, 138 \pm 7, 151 \pm 6 \text{ MeV}$, and in angular bins of 5° width.

Peaks are evident in the (γ, p) spectra corresponding to population of groups of low-lying states of ^{11}B at $E_x \sim 0, \sim 7, \text{ and } \sim 13 \text{ MeV}$. An example is shown in Fig. 1. In order to estimate the cross section leading to these states, a Gaussian-fitting procedure was used. Gaussians of width 3.8 MeV FWHM, in accordance with the experimental resolution, were fitted to the (γ, p) spectra. The Gaussian centroids were restricted to the energy ranges $E_x = 0-1.5, 6.5-8.0, \text{ and } 12.0-13.5 \text{ MeV}$, where resolvable peaks were observed. These values of E_x correspond to known groups of energy levels in ^{11}B , and allow for variations in the calibrated energy scale and relative strengths of the contributing states, as a function of proton angle. As well as these three resolvable peaks, there is strength in the spectra at higher values of E_x , corresponding to the population of higher energy states in ^{11}B , and the

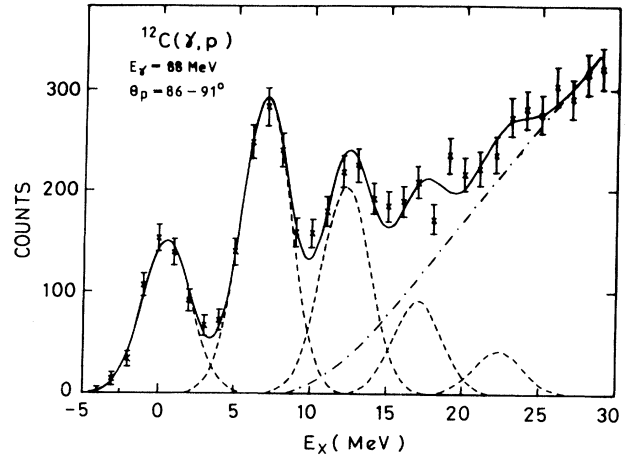


FIG. 1. The E_x spectrum for the $^{12}\text{C}(\gamma, p)^{11}\text{B}$ reaction at $\bar{E}_\gamma = 88 \text{ MeV}$ and c.m. angles of $\theta_p = 86^\circ-91^\circ$. The Gaussians and QD continuum region were fitted as described in the text, and are represented by the dashed and dot-dashed lines, respectively. The sum of the fitted curves is represented by the solid line.

quasideuteron (QD) breakup region. No attempt was made to determine the cross section for these higher regions of E_x , but further Gaussians were fitted at $E_x = 17-18, 21-23$, together with a broader Gaussian above $E_x = 45 \text{ MeV}$, and a QD continuum, in order to provide a good overall fit to the spectra. The continuum region was calculated using a QD model as described in Ref. [19], with the absolute magnitude allowed to vary as a free parameter in the fit. Previous calculations of this type for the $^{12}\text{C}(\gamma, pn)$ reaction have been quite successful in reproducing the shape of both proton and neutron spectra [2,20].

It can be seen in Fig. 1 that the fit provides a good representation of the spectrum shape, allowing an accurate determination of the cross section up to $E_x \simeq 13 \text{ MeV}$. The greatest uncertainty occurs for the $\sim 13 \text{ MeV}$ peak, for which the area depends strongly on the calculated QD continuum. An estimate of the uncertainty for this peak was made by assuming that the calculated QD continuum and Gaussian at $E_x = 17-18 \text{ MeV}$ could be in error by as much as 50%. This additional error from the fitting procedure was added in quadrature to the statistical error for each data point.

The accuracy of the absolute determination of the $^{12}\text{C}(\gamma, p)$ differential cross section was tested by measuring the protons from the $^2\text{H}(\gamma, p)$ reaction using the CD_2 target. Comparing the cross section determined from these data with parametrizations of previous results [21], there is agreement to within about 10%. This is similar to the level of agreement amongst the parametrizations themselves. From this comparison, the systematic uncertainty in the cross sections has been estimated to be $\pm 10\%$.

The $^{12}\text{C}(\gamma, p)^{11}\text{B}$ differential cross-section values for the three lowest fitted regions in the E_x spectra are shown in Table I, for each photon energy bin, and plotted as crosses in Figs. 2-5.

The data are compared in Fig. 2(a) with previous $^{12}\text{C}(\gamma, p_{0+1})^{11}\text{B}$ data from Tohoku University [1] (solid circles), obtained using a ΔE - E detector, for a tagged photon energy bin centered on 88 MeV. The Tohoku data, which have a quoted systematic uncertainty of 10%, are in good agreement with the present data. In further comparisons with previous data, shown in Fig. 2, the $E_\gamma = 88$ and 106 MeV data are compared with the

$^{12}\text{C}(\gamma, p_{0+1})^{11}\text{B}$ data from Matthews *et al.* [7] at $E_\gamma = 80$ and 100 MeV (squares), from McGeorge *et al.* [2] at $E_\gamma = 80$ MeV (diamonds), and the proton-capture data of Höistad *et al.* [10] at an equivalent photon energy of 105.9 MeV (circles). The quoted systematic errors of these experiments are 22%, 15%, and 8%, respectively. Since the data sets of Matthews *et al.* and McGeorge *et al.* are at $E_\gamma = 80$ MeV, they have been rescaled by a fac-

TABLE I. Differential cross sections in the c.m. frame for the reaction $^{12}\text{C}(\gamma, p)^{11}\text{B}$ leading to specific excitation energy regions in the residual ^{11}B nucleus.

θ_p (deg) (c.m.)	$d\sigma/d\Omega_{\text{c.m.}}$ ($\mu\text{b}/\text{sr}$)				
	88 MeV	106 MeV	123 MeV	138 MeV	151 MeV
$E_x \simeq 0$ MeV region					
58.2	9.85 ± 0.27	3.83 ± 0.18	1.72 ± 0.14	0.72 ± 0.09	0.79 ± 0.10
63.3	7.75 ± 0.22	2.84 ± 0.16	1.19 ± 0.10	0.47 ± 0.08	0.30 ± 0.08
68.4	5.82 ± 0.20	1.99 ± 0.12	0.86 ± 0.10	0.35 ± 0.06	0.13 ± 0.05
73.4	4.26 ± 0.18	1.39 ± 0.12	0.50 ± 0.09	0.24 ± 0.06	0.17 ± 0.06
78.4	3.42 ± 0.15	0.98 ± 0.10	0.39 ± 0.08	0.24 ± 0.04	0.07 ± 0.04
83.5	2.49 ± 0.13	0.70 ± 0.09	0.31 ± 0.06	0.19 ± 0.04	0.06 ± 0.04
88.5	1.80 ± 0.12	0.45 ± 0.08	0.23 ± 0.07	0.11 ± 0.05	0.01 ± 0.03
93.5	1.28 ± 0.10	0.32 ± 0.06	0.15 ± 0.06	0.10 ± 0.04	0.06 ± 0.02
98.5	0.99 ± 0.10	0.19 ± 0.06	0.20 ± 0.04	0.03 ± 0.03	0.03 ± 0.02
103.4	0.61 ± 0.08	0.16 ± 0.06	0.09 ± 0.05	0.05 ± 0.02	0.01 ± 0.01
108.4	0.45 ± 0.07	0.12 ± 0.06	0.05 ± 0.04	0.05 ± 0.03	0.03 ± 0.02
113.4	0.34 ± 0.06	0.01 ± 0.04	0.05 ± 0.04	0.01 ± 0.04	0.02 ± 0.02
118.3	0.28 ± 0.07	0.10 ± 0.04	0.01 ± 0.05	0.06 ± 0.02	0.01 ± 0.03
123.3	0.03 ± 0.08	0.01 ± 0.04	0.07 ± 0.03	0.04 ± 0.03	0.01 ± 0.03
128.2	0.17 ± 0.07	0.09 ± 0.05	0.01 ± 0.05	0.06 ± 0.03	0.01 ± 0.03
$E_x \simeq 7$ MeV region					
58.3	6.80 ± 0.23	4.26 ± 0.20	2.76 ± 0.17	1.89 ± 0.13	1.29 ± 0.13
63.3	6.08 ± 0.21	3.60 ± 0.17	2.29 ± 0.15	1.35 ± 0.10	1.26 ± 0.10
68.4	5.48 ± 0.19	3.31 ± 0.16	1.92 ± 0.15	1.41 ± 0.10	0.90 ± 0.09
73.5	4.36 ± 0.18	2.57 ± 0.13	1.80 ± 0.11	0.99 ± 0.09	0.85 ± 0.09
78.5	4.07 ± 0.17	2.35 ± 0.13	1.31 ± 0.11	0.87 ± 0.08	0.45 ± 0.08
83.5	3.66 ± 0.16	2.08 ± 0.12	1.14 ± 0.10	0.74 ± 0.07	0.64 ± 0.07
88.5	3.60 ± 0.15	1.84 ± 0.12	1.11 ± 0.09	0.70 ± 0.07	0.47 ± 0.06
93.5	3.22 ± 0.14	1.47 ± 0.10	0.87 ± 0.09	0.59 ± 0.07	0.32 ± 0.06
98.5	2.73 ± 0.13	1.32 ± 0.10	0.79 ± 0.08	0.40 ± 0.05	0.29 ± 0.05
103.5	2.20 ± 0.13	1.40 ± 0.09	0.58 ± 0.08	0.28 ± 0.05	0.26 ± 0.05
108.5	1.82 ± 0.11	0.93 ± 0.08	0.49 ± 0.08	0.22 ± 0.04	0.16 ± 0.05
113.4	1.59 ± 0.11	0.75 ± 0.08	0.45 ± 0.07	0.15 ± 0.05	0.08 ± 0.04
118.4	1.64 ± 0.10	0.76 ± 0.08	0.42 ± 0.06	0.22 ± 0.05	0.07 ± 0.04
123.3	1.35 ± 0.10	0.65 ± 0.08	0.29 ± 0.06	0.20 ± 0.05	0.08 ± 0.03
128.2	1.46 ± 0.12	0.52 ± 0.08	0.28 ± 0.07	0.16 ± 0.04	0.08 ± 0.03
$E_x \simeq 13$ MeV region					
58.3	4.47 ± 0.55	2.41 ± 0.40	2.21 ± 0.19	1.48 ± 0.16	0.94 ± 0.16
63.4	3.63 ± 0.50	1.86 ± 0.37	1.67 ± 0.20	1.24 ± 0.13	0.95 ± 0.13
68.4	3.18 ± 0.48	1.89 ± 0.37	1.46 ± 0.19	0.89 ± 0.15	0.60 ± 0.12
73.5	3.38 ± 0.35	1.72 ± 0.29	1.07 ± 0.21	0.75 ± 0.14	0.66 ± 0.12
78.5	2.39 ± 0.39	1.23 ± 0.34	0.95 ± 0.16	0.71 ± 0.13	0.51 ± 0.10
83.5	2.41 ± 0.34	1.11 ± 0.26	0.86 ± 0.16	0.56 ± 0.12	0.38 ± 0.12
88.6	2.51 ± 0.30	1.11 ± 0.26	0.80 ± 0.18	0.49 ± 0.10	0.45 ± 0.07
93.6	1.93 ± 0.31	0.91 ± 0.22	0.78 ± 0.15	0.48 ± 0.09	0.28 ± 0.09
98.5	1.72 ± 0.26	0.75 ± 0.23	0.53 ± 0.15	0.40 ± 0.09	0.26 ± 0.07
103.5	1.46 ± 0.26	0.74 ± 0.21	0.59 ± 0.13	0.22 ± 0.10	0.22 ± 0.07
108.5	1.29 ± 0.22	0.69 ± 0.17	0.41 ± 0.13	0.17 ± 0.09	0.32 ± 0.06
113.4	1.26 ± 0.20	0.47 ± 0.17	0.21 ± 0.15	0.23 ± 0.07	0.20 ± 0.07
118.4	1.06 ± 0.24	0.42 ± 0.16	0.19 ± 0.13	0.09 ± 0.10	0.22 ± 0.06
123.3	1.05 ± 0.19	0.60 ± 0.12	0.51 ± 0.10	0.13 ± 0.08	0.22 ± 0.06
128.2	1.00 ± 0.16	0.49 ± 0.15	0.42 ± 0.12	0.19 ± 0.09	0.14 ± 0.06

tor of 0.62, which describes the cross-section dependence of the present data for an 8 MeV photon energy shift. Likewise for the $E_\gamma = 106$ MeV comparison, the $E_\gamma = 100$ MeV Matthews *et al.* data have been rescaled by a factor of 0.7, to correct for the 6 MeV discrepancy in photon energy. The proton-capture data are for the ground-state cross section, and so have been rescaled by a factor of 1.27, since the present data include the cross section to the first excited state. Previous experiments [4,5,7] have shown that population of the first excited state of ^{11}B is $\sim 27\%$ as probable as population of the ground state, for similar photon energies to those used here.

The comparisons shown in Fig. 2 show that there are some discrepancies between the data sets. The McGeorge *et al.* data show a different angular dependence to the present data, and the data sets of Matthews *et al.* and Höistad *et al.* differ from the present data by angle- and energy-independent factors of 1.6 ± 0.2 and 0.7 ± 0.1 , respectively. These discrepancies are much larger than

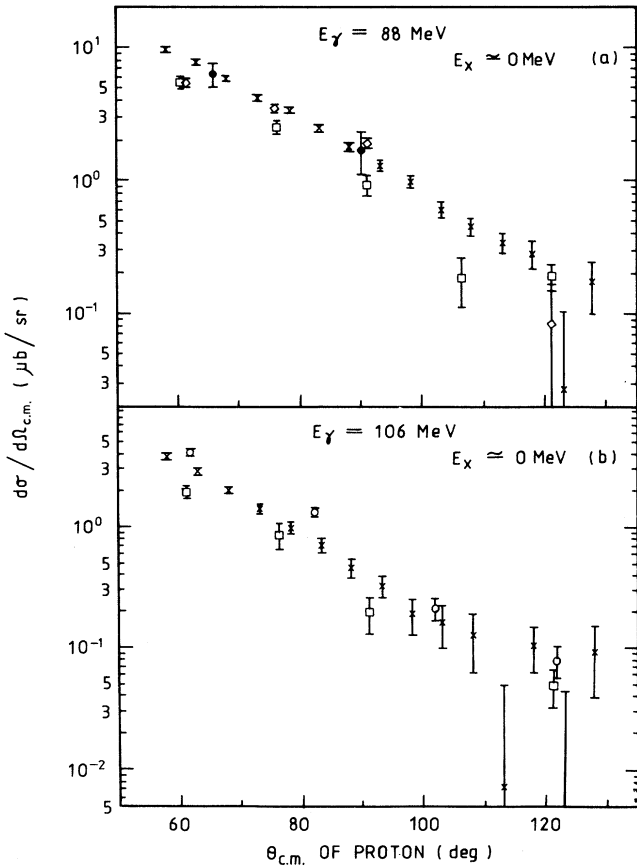


FIG. 2. Comparison of the present data to previous data sets from Tohoku [1] (solid circles), Matthews *et al.* [7] (squares), McGeorge *et al.* [2] (diamonds), and Höistad *et al.* [10] (circles). The previous data sets have been corrected for their different photon energies by applying scaling factors, as described in the text. The errors shown are statistical only. The quoted systematic errors associated with the present data and with each previous data set are 10%, 10%, 22%, 15%, and 8%, respectively.

would be expected from the quoted systematic errors of the experiments.

The reasons for the discrepancies between the data sets are not clear, but very different techniques were used to collect the data. The Matthews *et al.* data were obtained using the single-difference bremsstrahlung unfolding technique. The uncertainties involved in this technique are quite large, as discussed in the Appendix of Ref. [7]. The proton-capture data of Höistad *et al.* have the smallest quoted systematic error of $\pm 8\%$, and their method has no obvious weak point. The other measurements in Fig. 2, from Tohoku, McGeorge *et al.*, and the present data, all used tagged photons and would therefore be expected to give reliable absolute magnitudes.

As the data of Matthews *et al.* are low compared to the other data sets, it is instructive to compare the data at

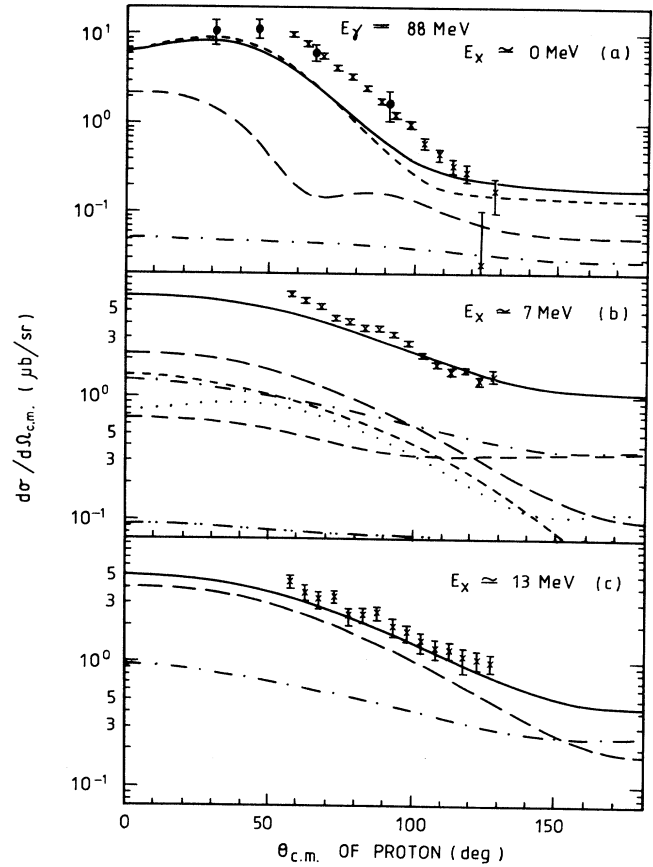
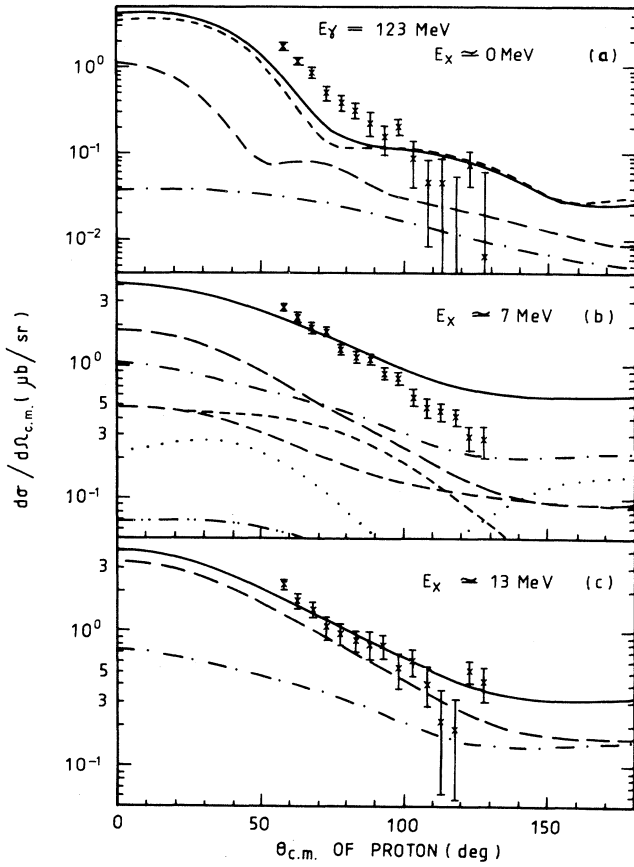
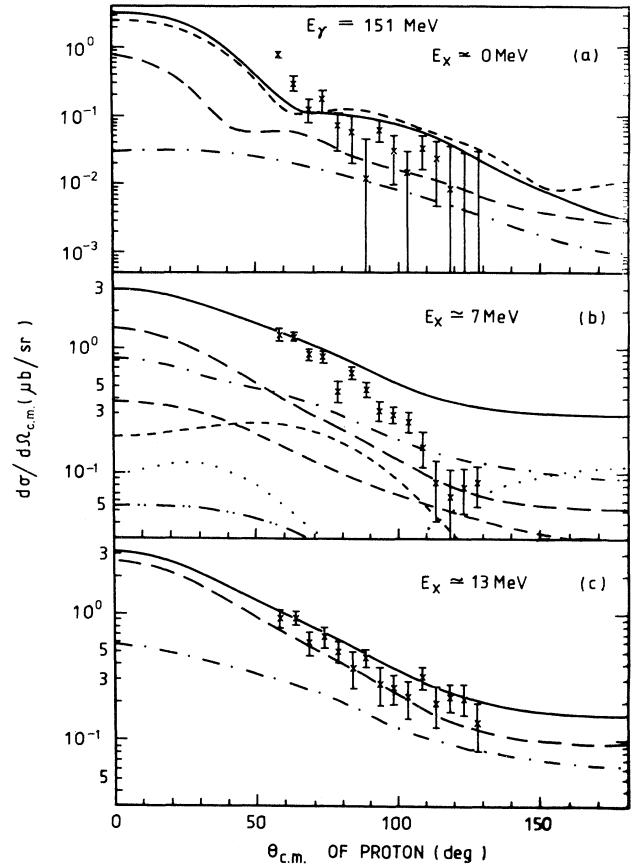


FIG. 3. Differential cross sections for $^{12}\text{C}(\gamma, p)^{11}\text{B}$ at $\bar{E}_\gamma = 88$ MeV leading to specific excitation energies in the residual ^{11}B nucleus of (a) ~ 0 MeV, (b) ~ 7 MeV, and (c) ~ 13 MeV. The crosses are the present data and the solid circles are data from Tohoku [1]. Both data sets have an additional systematic uncertainty of 10%, which is not shown. The curves are calculations as described in the text, (a) DKO (long dashed), 1h (short dashed), 2h1p (dot-dashed), coherent sum of 1h and 2h1p (solid curve); (b) and (c) 2h1p calculations for the states: $\frac{3}{2}^-$ (dot-dot-dashed), $\frac{5}{2}^-$ (short dashed), $\frac{7}{2}^-$ (medium dashed), $\frac{1}{2}^+$ (negligible), $\frac{3}{2}^+$ (dotted), $\frac{5}{2}^+$ (dot-dashed), $\frac{7}{2}^+$ (long-dashed), and incoherent sum (solid).

FIG. 4. As in Fig. 3, but at $\bar{E}_\gamma = 123$ MeV.FIG. 5. As in Fig. 3, but at $\bar{E}_\gamma = 151$ MeV.

lower energies to see if such a trend is apparent there as well. Some previous data sets [3,4,6] were normalized to the Matthews *et al.* data and so do not provide a useful comparison. For those that were not normalized, a comparison has been made in Table II. The comparison is for $\theta_{c.m.} = 91^\circ$ at $E_\gamma = 60$ and 80 MeV. It is clear that at these lower photon energies there are different discrepancies, which prevent a consistent set of experiments from being identified.

IV. CROSS SECTION CALCULATIONS

In Figs. 3–5 the data have been compared with calculations which are similar in nature to those previously published by Ryckebusch *et al.* [13,14] for lower photon energies. The calculations can be categorized into four distinct types, whose characteristics are described below, followed by a discussion of some features common to the calculations.

TABLE II. Differential cross sections in the c.m. frame for the reaction $^{12}\text{C}(\gamma, p_{0+1})^{11}\text{B}$ for five different experiments.

E_γ (MeV)	θ_p (deg) (c.m.)	Experiment	$d\sigma/d\Omega_{c.m.}$ ($\mu\text{b}/\text{sr}$)	Systematic error quoted
60	91	Matthews <i>et al.</i> [7]	12 ± 1	$\pm 22\%$
		Tohoku [1]	10 ± 1	$\pm 10\%$
		McGeorge <i>et al.</i> [2]	13 ± 2	$\pm 15\%$
		Van Hoorebeke <i>et al.</i> [5]	16 ± 1	$\pm 15\%$
80	91	Matthews <i>et al.</i> [7]	1.5 ± 0.3	$\pm 22\%$
		Tohoku [1]	1.9 ± 0.4	$\pm 10\%$
		McGeorge <i>et al.</i> [2]	3.1 ± 0.5	$\pm 15\%$
		Van Hoorebeke <i>et al.</i> [5]	2.6 ± 0.3	$\pm 15\%$
		Present data extrapolated	2.5 ± 0.1	$\pm 10\%$

(1) The first is based on a DKO model, using the one-body current form of the impulse approximation (IA), i.e., the sum of the convection and the magnetization current. In these DKO calculations the distortions in the outgoing particle wave are accounted for. As described in Ref. [13], a self-consistent Hartree-Fock formalism is used to calculate the bound-state wave functions, the phase shifts, and the partial waves of the escaping particle wave function. Results of this DKO calculation for the $E_x \simeq 0$ MeV region are plotted in Figs. 3(a)–5(a) as the long-dashed curves.

(2) The second is an RPA calculation of single-hole transition matrix elements, using an effective Skyrme NN interaction. This calculation incorporates exchange currents and multistep processes and has been described in Ref. [13]. In order to achieve consistency in the RPA calculations both the exchange currents and the multistep processes are generated through the effective NN interaction. Current contributions which go beyond the IA are generated by performing minimal substitution in the Skyrme effective NN Hamiltonian [22]. In this way the gauge invariant character of the RPA calculations is preserved. The RPA calculations will be referred to as the $1h$ calculation, and results for the $E_x \simeq 0$ MeV region are plotted in Figs. 3(a)–5(a) as the short-dashed curves.

(3) The third type of calculation is of slightly different nature. From earlier high-resolution $^{12}\text{C}(\gamma, p)$ experiments [4,5] it was apparent that the proton spectra looked quite different from the spectra obtained in related reactions like $(d, ^3\text{He})$ and quasielastic $(e, e'p)$. In particular, the (γ, p) results pointed towards a strong excitation of an unresolved triplet of states $(\frac{1}{2}^+, \frac{5}{2}^+, \frac{7}{2}^-)$ around 7 MeV excitation energy in ^{11}B . This triplet of states is known to carry very little $1h$ strength [23], and in Ref. [14] its strong excitation was interpreted to be the result of a direct photoproton knockout process after photoabsorption on a pion, leaving the residual nucleus in a $2h1p$ state. In the calculations only the diagrams where the photon couples to a charged pion (seagull and pion-in-flight diagrams) are retained. The bound and the escaping proton waves are calculated as described in (1). It should be stressed that the excitation of the $2h1p$ states is interpreted here as a purely pion exchange current effect. The results of these $2h1p$ calculations for the three lowest fitted regions are plotted in Figs. 3(a)–5(a) as the dot-dashed curves.

(4) The fourth calculation is a coherent sum of $1h$ and $2h1p$ calculations, and results for the $E_x \simeq 0$ MeV region are plotted in Figs. 3(a)–5(a) as the solid curves.

Some features of the different calculations are common, and these will now be discussed. As outlined in Ref. [14], the ground state ($J^\pi = \frac{3}{2}^-$) of ^{11}B has been assumed to have the structure

$$\alpha|0^+(\text{g.s.}) \otimes (1p)_{\pi}^{-1}\rangle + \beta|2_1^+(4.44 \text{ MeV}) \otimes (1p)_{\pi}^{-1}\rangle, \quad (2)$$

where the first term represents the pure $1h$ state, built on the ground state of ^{12}C , and the second term represents a $2h1p$ state, built on the first excited state of ^{12}C . The wave function amplitudes α and β determine the relative strengths of the $1h$ and $2h1p$ contributions. The values

of α and β used in the calculation of the ground-state $^{12}\text{C}(\gamma, p)$ cross section were 0.69 and 0.31, respectively. The $1h$ amplitude α was obtained from spectroscopic factors extracted from an $(e, e'p)$ experiment by van der Steenhoven *et al.* [23].

In the $2h1p$ calculations of the cross section to the excited states of the residual ^{11}B nucleus, a configuration of $|((1p_{\frac{3}{2}})^{-1}1p_{\frac{1}{2}})_{\nu}(1p_{\frac{3}{2}})_{\pi}^{-1}; \frac{3}{2}^-, \frac{5}{2}^-, \frac{7}{2}^-\rangle$ was assumed for those states with negative parity and the configuration $|((1p_{\frac{3}{2}})^{-1}1d_{\frac{5}{2}})_{\nu}(1p_{\frac{3}{2}})_{\pi}^{-1}; \frac{1}{2}^+, \frac{3}{2}^+, \frac{5}{2}^+, \frac{7}{2}^+\rangle$ for the positive parity states, as in Ref. [14]. It can be expected that these would be the leading $2h1p$ configurations in the lower excitation part of the ^{11}B spectrum. The alternative $|((1p_{\frac{3}{2}})^{-1}2s_{\frac{1}{2}})_{\nu}(1p_{\frac{3}{2}})_{\pi}^{-1}; \frac{1}{2}^+, \frac{3}{2}^+, \frac{5}{2}^+, \frac{7}{2}^+\rangle$ configuration was investigated as well, but was found to produce much smaller (γ, p) cross sections than the $|((1p_{\frac{3}{2}})^{-1}1d_{\frac{5}{2}})_{\nu}(1p_{\frac{3}{2}})_{\pi}^{-1}; \frac{1}{2}^+, \frac{3}{2}^+, \frac{5}{2}^+, \frac{7}{2}^+\rangle$ configuration.

In order to compare the calculations with the measured cross sections, it is necessary to identify which specific states in the residual ^{11}B nucleus are covered by the peaks. At $E_x \simeq 7$ MeV excitation in ^{11}B there are both positive and negative parity states in the range of energies covered by the peak. Calculations were performed for the following states, summing all the contributions incoherently, using the squared wave function amplitudes given in parentheses: $\frac{3}{2}^-$ (0.1), $\frac{5}{2}^-$ (0.29), $\frac{7}{2}^-$ (0.26), $\frac{1}{2}^+$ (0.3), $\frac{3}{2}^+$ (0.5), $\frac{5}{2}^+$ (0.38), and $\frac{7}{2}^+$ (0.28). For the $\frac{5}{2}^-$, $\frac{7}{2}^-$, $\frac{1}{2}^+$, and $\frac{5}{2}^+$ states the squared wave function amplitudes were chosen on the basis of large-scale shell-model calculations, as described in Ref. [14]. For the other states contributing to the $E_x \simeq 7$ MeV region similar shell-model calculations were unavailable, and so the squared amplitudes were allowed to vary between 0.1 and 0.5, until a best global fit was obtained to the data over the full range of energies and angles. The resulting curves calculated by this method are shown in Figs. 3(b)–5(b). The seven separate contributions are shown multiplied by the squared wave function amplitudes quoted above. The incoherent sum of the seven contributions is shown as the solid curve in each figure.

Similarly for the $E_x \simeq 13$ MeV peak, $2h1p$ calculations were performed for the states $\frac{5}{2}^+$ and $\frac{7}{2}^+$, summing the two contributions incoherently, with squared amplitudes of 0.26 and 0.5, respectively, which gave a best global fit to the data. The calculated curves are shown in Figs. 3(c)–5(c).

It is clear from the comparison of the data and calculations that for the $E_x \simeq 0$ MeV region, the best agreement is obtained when both $1h$ and $2h1p$ contributions are included, although the $2h1p$ contribution has only a small effect. The DKO calculation fails badly to reproduce the cross sections at any energy or angle. The calculations are only for the ground-state cross section, while the $E_x \simeq 0$ MeV peak in the data includes the cross section to the $\frac{1}{2}^-$ state at 2.12 MeV in ^{11}B . Population of this $\frac{1}{2}^-$ state has previously been observed to be only about 27% as probable [4,5,7], so cannot explain the discrepancy between the data and theory, which is about a factor of 2 at 88 MeV.

For the $E_x \simeq 7$ MeV region, the $2h1p$ calculations do not correctly describe the forward peaking of the angular distribution. The agreement at forward angles might be improved by the inclusion of $1h$ contributions for this peak, but previous calculations [14] have indicated that $1h$ contributions are insignificant compared to $2h1p$ contributions for this energy region. Another possibility is that the relative strengths of the contributing states have been wrongly estimated in the calculations. This was tested by allowing the squared amplitudes of the seven contributing states to vary as free parameters in the range from 0.1 to 0.5. The best global fit was obtained when the $\frac{5}{2}^-$, $\frac{3}{2}^+$, and $\frac{7}{2}^+$ states had squared amplitudes of 0.50, 0.50, and 0.44, respectively, with 0.10 for all the other states.

In the case of the $E_x \simeq 13$ MeV peak, there is very good agreement between the data and calculations for the whole photon energy range, at all angles. Of all of the most likely $2h1p$ configurations in ^{11}B , the $|((1p_{3/2})^{-1}1d_{3/2})_{\nu}, (1p_{3/2})_{\pi}^{-1}, \frac{5}{2}^+, \frac{7}{2}^+ \rangle$ configurations are found to produce the largest (γ, p) cross sections in our one-pion exchange model. In Ref. [14] it was pointed out that the $\frac{5}{2}^+$ configuration is the leading contribution to the unresolved 7 MeV triplet in ^{11}B . It now turns out that also the $E_x=13$ MeV peak can be well described in terms of a mesonic excitation of these dominant $2h1p$ configurations. This suggests that the pion-exchange currents have an important role in the photoabsorption process and that photoabsorption on these currents has a tendency to excite some particular $2h1p$ states in exclusive (γ, p) processes. Not all of the $2h1p$ configurations are equally excited, as there is a strong dependence of the cross sections on the detailed shell-model structure of the $2h1p$ configuration.

V. "SCALING" ANALYSIS

In some previous analyses of $^{12}\text{C}(\gamma, p)^{11}\text{B}$ data, it has been demonstrated [24,4] that the data scale with momentum mismatch $\hbar\mathbf{q}_m$, defined by

$$\mathbf{q}_m = \mathbf{k}'_p - \left(1 - \frac{1}{A}\right) \mathbf{k}_\gamma, \quad (3)$$

where $\hbar\mathbf{k}'_p$ is the internal center-of-mass (c.m.) momentum of the outgoing proton before it emerges from the nuclear potential well and $\hbar\mathbf{k}_\gamma$ is the c.m. photon momentum. Findlay and Owens first showed for ^{16}O [25] and then for ^{12}C [24] that if the DKO mechanism is assumed, it is possible to obtain a $1p$ momentum distribution from (γ, p_0) data. In the $^{12}\text{C}(\gamma, p_0)$ paper they treated distortion in the final state approximately, assuming that

$$(\hbar\mathbf{k}'_p)^2 = (\hbar\mathbf{k}_p)^2 - \left(1 - \frac{1}{A}\right) 2m_p V(E), \quad (4)$$

where $\hbar\mathbf{k}_p$ is the observed outgoing c.m. proton momentum, m_p is the proton mass, and $V(E) = V_0[1 - 1.015 \tanh(0.005E)]$, with $V_0 = 33.5$ MeV, is the depth of the final state potential. The momentum density $\frac{1}{4\pi}|Q(q)|^2$ was then extracted from the data using the

relation

$$\frac{d\sigma}{d\Omega} = 2\pi^2 \left(1 - \frac{1}{A}\right) \frac{e^2}{m_p c^2} \frac{k k'^2}{k_\gamma} \left(1 - \frac{\partial V}{\partial E}\right) \times \eta \sin^2 \theta \frac{1}{4\pi} |Q(q)|^2, \quad (5)$$

where $\frac{d\sigma}{d\Omega}$ is the c.m. differential cross section, θ is the c.m. angle of proton emission, $(1 - \frac{\partial V}{\partial E})$ is the Perey factor, and η is an energy-independent absorption factor, which was 0.7 in the analysis of both $^{12}\text{C}(\gamma, p)$ and $^{12}\text{C}(e, e'p)$ data by Findlay and Owens [24]. The momentum density distributions were found to agree well with the distributions derived from $^{12}\text{C}(e, e'p)$ data and with an Elton-Swift [26] single particle wave function. However, analyses in a recent paper [27] indicate that momentum distributions derived from $(e, e'p)$ data do not connect smoothly with those from (γ, p) data. This will only be conclusively tested when $(e, e'p)$ data at high momentum mismatch are published.

It has recently been shown in Refs. [28,29] that scaling of the cross section with momentum mismatch is consistent with both $1N$ and $2N$ photon absorption mechanisms. In Ref. [28] the photoreaction matrix element was expanded into $1N$ and $2N$ terms, using a short-range correlation function, which represents the effect of mutual repulsion between a nucleon pair. Various simple forms were used for the correlation function, giving reasonable agreement with $^{16}\text{O}(\gamma, p_0)$ data for a delta function and also for a form based on the difference between two Gaussians.

Using the same equations and parameters as in Refs. [24,28], momentum density distributions were extracted for the present data. The results are shown in Fig. 6. The dashed curve in the figure is the $1p_{3/2}$ momentum distribution calculated from Elton-Swift [26] potential parameters. The dot-dashed curve represents the $2N$ mechanism, calculated using the formalism of Ref. [28], with Elton-Swift potential parameters for the three overlapping momentum wave functions and a delta function as the correlation function, with a wound volume corresponding to $r_c = 0.8$ fm. The solid curve represents the result of adding the $1N$ and $2N$ amplitudes together, assuming a zero phase difference between them.

As seen in Fig. 6, the data scale well with momentum mismatch over the wide photon energy and angular range of the experiment. Over this range the data vary by three orders of magnitude, yet only minor deviations from a smooth curve are seen in Fig. 6. The $1p_{3/2}$ single particle wave function describes the general trend of the extracted momentum density, but is too small to allow an explanation of the observed cross section as a DKO process. This observation is in conformity with the results of the DKO calculations which were presented in the previous chapter. Inclusion of the $2N$ term, as described above, provides satisfactory agreement between the present data and calculated momentum density, except in the region around $\hbar q_m \simeq 490$ MeV/c, where the momentum density extracted from the data decreases smoothly as a function of momentum mismatch, rather than following the first minimum in the momentum wave function. The absence

of a deep minimum in the data can be explained by distortions in the final state, which are not accounted for in the plane-wave calculations described above.

For the $E_x \simeq 7$ and ~ 13 MeV regions of residual excitation, the momentum distributions extracted from the data have similar slopes, both smaller than that for the $E_x \simeq 0$ MeV region, as can be seen in Fig. 6. This effect has been previously observed for the $E_x \simeq 7$ MeV region in Ref. [4], where separate momentum distributions that were obtained for the ground state, 2.1, and 5 MeV regions had significantly steeper slopes than that for the ~ 7 MeV region. It is consistent with the calculations of Ref. [14] and Sec. IV, which show an increasing importance of $2h1p$ contributions compared to $1h$ contributions for regions at higher E_x , and also that the $2h1p$ angular distributions, which are interpreted here as a predominantly pion exchange current effect, are much less steep than those predicted for the $1h$ contribution.

VI. CONCLUSIONS

New tagged-photon data on the $^{12}\text{C}(\gamma, p)^{11}\text{B}$ reaction have been presented for the photon energy range 80–157 MeV. The energy resolution of 3.5 MeV allowed the cross section to three groups of states in the residual ^{11}B nucleus at $E_x \simeq 0, 7,$ and 13 MeV to be measured. Comparisons of the present data with some earlier data sets for the $E_x \simeq 0$ MeV cross section, as seen in Fig. 2 and Fig. 3(a), show some agreements but also that there are some discrepancies, which are larger than the quoted systematic errors.

Comparison between the $E_x \simeq 0$ MeV cross-section data and calculations described in Sec. IV, shown in Figs. 3–5, show that the DKO model calculations do not account for the cross-section angular distributions. The data are better described by an RPA model that includes multistep processes and MEC that lead to $1h$ states in ^{11}B . For the ground state cross section the $1h$ contribution is much larger than the $2h1p$ contribution. The discrepancy between the full $1h + 2h1p$ RPA calculation and the data is as much as a factor of 2 at 88 MeV photon energy, as seen in Fig. 3(a).

Comparisons between the cross-section data for $E_x \simeq 7$ MeV and the $2h1p$ calculations of Sec. IV, shown in Figs. 3(b)–5(b), show that the data angular distributions are more forward-peaked than calculated. Of the seven contributions calculated for the cross section, the $\frac{5}{2}^-$, $\frac{3}{2}^+$, and $\frac{7}{2}^+$ states give angular distributions that most closely resemble the data.

For the $E_x \simeq 13$ MeV peak, the very good agreement between the data and the $2h1p$ calculations suggests that in excitation energy regions of ^{11}B where little $1h$ strength is located, the (γ, p) process is dominated by the pion exchange currents.

It has been demonstrated in Fig. 6 that the $^{12}\text{C}(\gamma, p)$ cross-section data scale well with momentum mismatch for each of the three residual excitation regions observed in the experiment. The scaling behavior observed here is over a range of momentum mismatch from 340 to 600 MeV/c, which is to higher values than previously pub-

lished on this nucleus [24,4]. Scaling is expected for both $1N$ and $2N$ absorption mechanisms, and so both the shape and magnitude of any calculated momentum density distribution are needed to decide which mechanism is favored by the data. The comparisons made in Fig. 6 indicate that the inclusion of both $1N$ and $2N$ absorption mechanisms is required to provide a satisfactory fit to the $E_x \simeq 0$ MeV data. The momentum density distribution extracted from the present data is more than a factor of 2 higher than the single particle wave function alone, indicating that a $1N$ absorption mechanism cannot account for the data.

For the $E_x \simeq 7$ and ~ 13 MeV regions of residual excitation, the slopes of the extracted momentum density distributions are lower than observed for the $E_x \simeq 0$ MeV region. This suggests that a $2N$ absorption mechanism plays a dominant role at the higher regions of E_x .

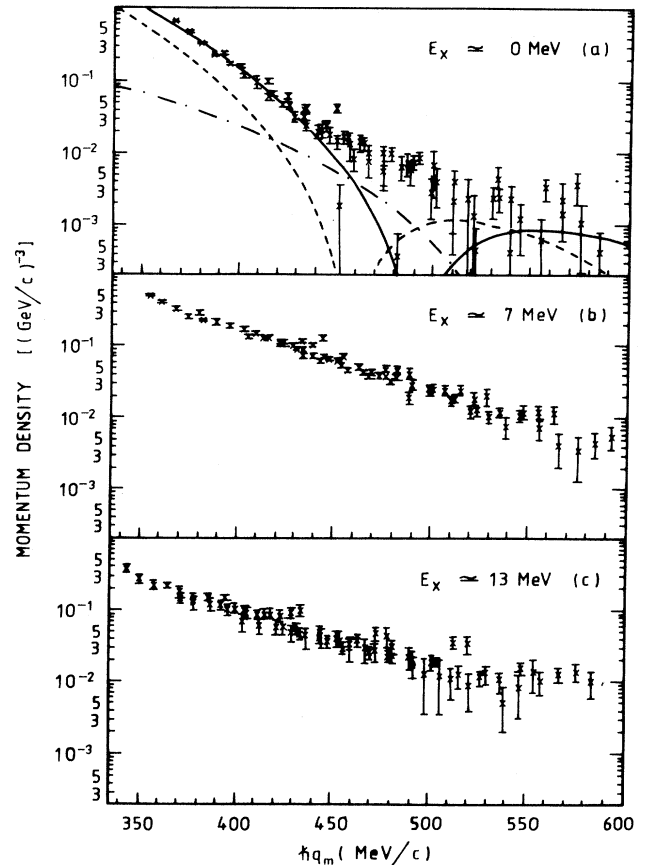


FIG. 6. Momentum density distributions for ^{12}C deduced from the cross-section data shown in Table I. The complete data set for photon energies $E_\gamma = 80$ –157 MeV has been used to obtain the distributions. The error bars shown are statistical only. The dashed curve in (a) is the $1p_{3/2}$ momentum distribution, the dot-dashed curve represents the $2N$ mechanism, and the solid curve represents the addition of $1N$ and $2N$ terms, as described in the text.

ACKNOWLEDGMENTS

The authors wish to thank the United Kingdom Science and Engineering Research Council and Deutsche Forschungsgemeinschaft (SFB201) for supporting this

work. The Institut für Kernphysik, Johannes-Gutenberg Universität is gratefully acknowledged for the use of its facilities and assistance during the course of the experiment.

-
- [1] K. Mori, Y. Fujii, T. Suda, I. Nomura, T. Terasawa, O. Konno, Y. Torizuka, P. D. Harty, G. J. O'Keefe, and K. Maeda, *Rep. Res. Lab. Nucl. Sci. Tohoku Univ.* **18**, 225 (1985).
- [2] J. C. McGeorge *et al.*, *Phys. Lett. B* **179**, 212 (1986).
- [3] A. C. Shotter, S. Springham, D. Branford, J. Yorkston, J. C. McGeorge, B. Schoch, and P. Jennewein, *Phys. Rev. C* **37**, 1354 (1988).
- [4] S. V. Springham *et al.*, *Nucl. Phys.* **A517**, 93 (1990).
- [5] L. Van Hoorebeke, Ph.D. thesis, University of Gent, Belgium, 1991; L. Van Hoorebeke *et al.*, *Phys. Rev. C* **42**, R1179 (1990); L. Van Hoorebeke, D. Ryckbosch, R. Van de Vyver, F. De Smet, J-O. Adler, B-E. Andersson, L. Isaksson, A. Sandell, B. Schröder, and K. Ziakas, *ibid.* **45**, 482 (1992).
- [6] D. G. Ireland *et al.*, *Nucl. Phys.* **A554**, 173 (1993).
- [7] J. L. Matthews, D. J. S. Findlay, S. N. Gardiner, and R. O. Owens, *Nucl. Phys.* **A267**, 51 (1976).
- [8] M. Anghinolfi *et al.*, *Nucl. Phys.* **A457**, 645 (1986).
- [9] H. J. Hausman, S. L. Blatt, T. R. Donoghue, J. Kalen, W. Kim, D. G. Marchlinski, T. W. Rackers, P. Schmalbrook, M. A. Kovash, and A. D. Bacher, *Phys. Rev. C* **37**, 503 (1988).
- [10] B. Höistad, E. Nilsson, J. Thun, S. Dahlgren, S. Isaksson, G. S. Adams, C. Landberg, T. B. Bright, and S. R. Cotanch, *Phys. Lett. B* **276**, 294 (1992).
- [11] M. Gari and H. Hebach, *Phys. Rep.* **72**, 1 (1981); H. Hebach, A. Wortberg, and M. Gari, *Nucl. Phys.* **A267**, 425 (1976).
- [12] M. Cavinato, M. Marangoni, P. L. Ottaviani, and A. M. Saruis, *Nucl. Phys.* **A373**, 445 (1982); M. Cavinato, M. Marangoni, and A. M. Saruis, *Nuovo Cimento A* **76**, 197 (1983); M. Cavinato, M. Marangoni, and A. M. Saruis, *Nucl. Phys.* **A422**, 237 (1984).
- [13] J. Ryckebusch, M. Waroquier, K. Heyde, J. Moreau, and D. Ryckbosch, *Nucl. Phys.* **A476**, 237 (1988).
- [14] J. Ryckebusch, K. Heyde, L. Machenil, D. Ryckbosch, M. Vanderhaeghen, and M. Waroquier, *Phys. Rev. C* **46**, R829 (1992).
- [15] J. D. Kellie *et al.*, *Nucl. Instrum. Methods A* **241**, 153 (1985).
- [16] I. J. D. MacGregor *et al.*, *Nucl. Phys.* **A533**, 269 (1991).
- [17] I. J. D. MacGregor *et al.*, *Nucl. Instrum. Methods A* **262**, 347 (1987).
- [18] R. O. Owens, *Nucl. Instrum. Methods A* **288**, 574 (1990).
- [19] P. D. Harty, I. J. D. MacGregor, J. C. McGeorge, S. N. Dancer, and R. O. Owens, *Phys. Rev. C* **47**, 2185 (1993).
- [20] P. D. Harty *et al.*, *Phys. Rev. C* **37**, 13 (1988).
- [21] P. Rossi *et al.*, *Phys. Rev. C* **40**, 2412 (1989); A. E. Thorlacius and H. W. Fearing, *ibid.* **33**, 1830 (1986); M. P. De Pascale *et al.*, *Phys. Lett.* **119B**, 30 (1982); D. A. Jenkins, P. T. Debevec, and P. D. Harty, *Phys. Rev. C* **50**, 74 (1994).
- [22] J. Ryckebusch, *Proceedings of the Workshop on Nuclear Physics with Real Photons below Pion Threshold*, Gent, 1989, p. 19 (unpublished).
- [23] G. van der Steenhoven, H. P. Blok, E. Jans, M. de Jong, L. Lapikas, E. N. M. Quint, and P. K. A. de Witt Huberts, *Nucl. Phys.* **A480**, 547 (1988); G. van der Steenhoven, H. P. Blok, E. Jans, L. Lapikas, E. N. M. Quint, and P. K. A. de Witt Huberts, *ibid.* **A484**, 445 (1988).
- [24] D. J. S. Findlay and R. O. Owens, *Nucl. Phys.* **A292**, 53 (1977).
- [25] D. J. S. Findlay and R. O. Owens, *Phys. Rev. Lett.* **37**, 674 (1976).
- [26] L. R. B. Elton and A. Swift, *Nucl. Phys.* **A94**, 52 (1967).
- [27] D. G. Ireland and G. van der Steenhoven, *Phys. Rev. C* **49**, 2182 (1994).
- [28] R. O. Owens, J. L. Matthews, and G. S. Adams, *J. Phys. G* **17**, 261 (1991).
- [29] H. Schmieden *et al.*, *Phys. Lett. B* **314**, 284 (1993).